Journal of Physics D: Applied Physics

Electro-thermal modelling of anode and cathode in micro-EDM

IOP PUBLISHING JOURNAL OF PHYSICS D: APPLIED PHYSICS

J. Phys. D: Appl. Phys. **40** (2007) 2513–2521 doi:10.1088/0022-3727/40/8/015

Electro-thermal modelling of anode and cathode in micro-EDM

S H Yeo, W Kurnia and P C Tan

School of Mechanical and Aerospace Engineering, Nanyang Technological University, 50 Nanyang Avenue, Singapore 639798

Received 17 November 2006, in final form 19 January 2007
Published 4 April 2007
Online at stacks.iop.org/JPhysD/40/2513

Abstract
Micro-electrical discharge machining is an evolution of conventional EDM used for fabricating three-dimensional complex micro-components and microstructure with high precision capabilities. However, due to the stochastic nature of the process, it has not been fully understood. This paper proposes an analytical model based on electro-thermal theory to estimate the geometrical dimensions of micro-crater. The model incorporates voltage, current and pulse-on-time during material removal to predict the temperature distribution on the workpiece as a result of single discharges in micro-EDM. It is assumed that the entire superheated area is ejected from the workpiece surface while only a small fraction of the molten area is expelled. For verification purposes, single discharge experiments using RC pulse generator are performed with pure tungsten as the electrode and AISI 4140 alloy steel as the workpiece. For the pulse-on-time range up to 1000 ns, the experimental and theoretical results are found to be in close agreement with average volume approximation errors of 2.7% and 6.6% for the anode and cathode, respectively.

(Some figures in this article are in colour only in the electronic version)

Nomenclature

α	Average thermal diffusivity ($m^2\,s^{-1}$)
C	Combination of fraction of energy and fraction of molten area
C_a	Combination of fraction of energy and fraction of molten area expelled in anode
C_c	Combination of fraction of energy and fraction of molten area expelled in cathode
C_p	Average specific heat ($J\,kg^{-1}\,K^{-1}$)
d	Crater diameter (μm)
erfc	Complementary error function
E	Complete elliptic integrals of the second kind
h	Crater depth (μm)
ierfc	Inverse erfc
I_a	Average current (A)
I_p	Peak current (A)
J_0	Bessel function of the first kind of zero order
J_1	Bessel function of the first kind of first order
K	Complete elliptic integrals of the first kind
K_t	Average thermal conductivity ($W\,m^{-1}\,K^{-1}$)
q	Heat flux ($W\,m^{-2}$)
R	Heat flux radius (μm)
R_a	Heat flux radius at anode (μm)
R_c	Heat flux radius at cathode (μm)
ρ	Average material density ($kg\,m^{-3}$)
t_d	Pulse-on-time (ns)
T	Temperature (K)
T_m	Melting temperature (K)
T_o	Ambient temperature (K)
V_{crater}	Crater volume (μm^3)
V_o	Open voltage (V)
V_a	Average voltage (V)

1. Introduction

The micro-EDM process is one of the most well-known techniques in micromachining. As material removal is realized without physical contact between the tool and workpiece, there is no force exerted on the workpiece, adding to the advantages of the micro-EDM in fabricating intricate micro-scale features [1]. The fabrication of an electrode with diameter 2.8 μm and micro-hole as small as 5 μm [2, 3] as well as a 42 μm micro-slit with a length 7 mm [4] has been reported. Further development of this technique will be crucial in fulfilling the needs of the micro system technology (MST) market, which is predicted to grow at a rate of 16% per year [5].

The material removal process in micro-EDM is very complex and stochastic in nature. It involves a combination of several disciplines such as electrodynamics, electromagnetics, thermodynamics and hydrodynamics [6]. It is almost impossible to present a simple and comprehensive theory which can explain the nature of the process in every detail. However, a reliable analytical model which is able to provide a good approximation of the material removal is essential. This approximation will provide a good guide for choosing the appropriate process parameters in the machining process. It will also help to provide a prediction on the material removal rate, tool wear ratio and surface integrity, which is useful in the process planning and control.

This paper proposes an analytical model based on the electro-thermal theory to estimate the geometrical dimension of the micro-crater produced from single discharges. The developed model is able to predict the temperature distribution using the average voltage, the average current and the pulse-on-time data obtained during the material removal process. The crater sizes at the cathode and anode as a result of single discharges are determined by taking into account the fraction of energy used as well as fraction of the molten area expelled from the material.

2. Literature review

The analytical modelling of conventional EDM process has been investigated by various researchers since 1971. Due to the process characteristics, the models can be divided into three sections, namely plasma channel, anode erosion and cathode erosion. The plasma channel model is basically used to approximate the state of plasma during electrical discharges. By knowing the state, an appropriate boundary condition for the anode and cathode models can be defined. It has been shown by Eubank *et al* [7] that the combination between these three sections is important to have numerical consistency between the theoretical and experimental results.

A comprehensive attempt to model the plasma channel was reported by Lhiaubet *et al* [8]. The properties of diatomic plasma were taken as a constant and the fluid dynamic equation was included in the model. Eubank *et al* [7] reported the variable mass cylindrical plasma which expands with time. For an EDM process with a current of 2.34 A, the temperature and pressure of the plasma channel are approximated to be 11 210 K and 54 bar after 6 μs. Another approximation of plasma channel for the micro-EDM process was reported by Dhanik and Joshi [9]. The calculations of plasma showed that the temperature and pressure were found to be in the range 8100 ± 1750 K and 6 to 8 bars, respectively.

The material removal model was mainly based on the electro-thermal mechanism where the material removal at the anode and cathode occurs as a result of an extremely high temperature due to the high intensity of current flowing through the plasma channel. Snoeys and Van Dijck [10] developed an electro-thermal model by utilizing a semi-infinite cylinder with a circular heat input. The power from the energy input was assumed to be equally divided for each electrode. This work was followed by Van Dijck and Dutre [11] using a two-dimensional heat flow model where the medium is bounded by an adiabatic cylindrical surface in the radial direction. Two cases, namely for finite and infinite z direction, were considered in the development. However, the calculation results using this model with the experimental parameters [12] give a MRR of 4.461 mm^3 min^{-1} for a voltage of 25 V and a current of 12.8 A, which is approximately 8.83 times larger than the experimental results.

Another approach using a semi-infinite cylinder with a disc heat source was reported by Beck [13, 14]. The surfaces beyond the disc heat source region were assumed to be insulated. By using constant thermal properties and constant heat flux, the temperature distribution in the material was expressed in dimensionless variables. Pandey and Jilani [15, 16] used a similar approach and assumed that the erosion will take place on the melting area of the electrodes. Dibitonto *et al* [12] used a point heat source for the cathode erosion and a circular heat source for the anode [17]. The models were verified by using experimental data and it was shown that the models were able to give a good approximation of the material removal for long discharge pulses and high current input.

Despite the availability of the aforementioned models, the differences between conventional EDM and micro-EDM have made a direct application of the models to the latter process inaccurate. In micro-EDM, where the discharge energy and the pulse-on-time are generally less than 500 W and 5 μs, respectively, the models tend to overestimate the temperature distribution which leads to erroneous approximation of the material removal. Dibitonto's model for the cathode erosion at 25 V voltage input, 2.34 A current input and 5.6 μs pulse-on-time resulted in the theoretical MRR of 13.82 mm^3 min^{-1} as compared with the experimental MRR of 0.3 mm^3 min^{-1}, giving a ratio of 46.07 [12]. Therefore, an analytical model specifically used for micro-EDM is still limited. An attempt in this direction has been reported by Dhanik and Joshi [9] for the development of plasma channel. However, no attempt has been made for the modelling of the anode and cathode erosion.

3. Electro-thermal modelling

In this paper, the analytical approach based on an electro-thermal material removal mechanism is used to develop the models for the anode and cathode erosion. A two-dimensional heat transfer for a material subjected to a disc heat source on its surface is used as the foundation for the model development. Empirical equations will be established to approximate the boundary conditions for determining the heat flux radius of the anode and cathode.

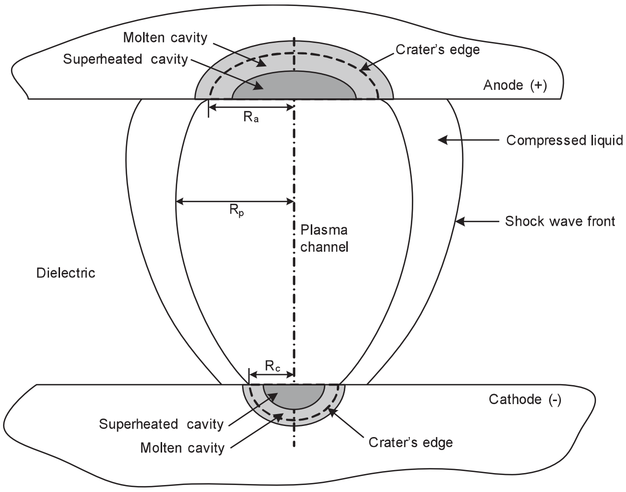

Figure 1. Schematic diagram of micro-EDM process.

Figure 1 illustrates the schematic diagram of the anode, cathode and plasma channel in the EDM process. The size of plasma radius at the cathode is smaller as compared with the anode as the cathode emits electrons while the anode emits positive ions. In addition, the mass of an electron is 9.11×10^{-31} kg while the mass of an ion is 1.67×10^{-27} kg, resulting in slower movement of ions as compared with the electrons [18]. Hence, the electrons will reach the anode first, followed by the cathode with one or two orders of magnitude delay in time [12]. Consequently, the anode will melt first resulting in a larger molten area as compared with the cathode, which is the general case in micro-EDM where pulse-on-time is short. As time progresses, the anode will begin to resolidify after a few microseconds due to the decrease in the local heat flux at the anode surface, while the molten area in the cathode is still expanding. Hence, the molten areas in anode will be smaller as compared with the cathode, which are prevalent in the conventional EDM.

Several simplifying assumptions are used for the model development. The main assumptions are the following.

1. Only one spark occurs for one discharge of energy input.
2. Average thermophysical properties are applied over the temperature range, from solid to liquid state.
3. Heat transfer to the electrode surface is dissipated only by conduction.
4. Radiation and convection heat losses are negligible.
5. Two-dimensional heat transfer.
6. The energy used for the material removal is only contributed by the voltage and current during pulse-on-time.
7. The Gaussian heat flux is simplified by an equivalent uniform heat flux.
8. The fraction of discharge energy going to the anode and cathode is taken as a constant.
9. The material in the superheated area is removed completely while only a constant fraction of the material in the molten area is removed.

In order to obtain the boundary conditions for the anode and cathode, the equivalent uniform heat flux radius for the anode and cathode are determined empirically using similar machining parameters in single discharge experiments. The energy distribution is considered to be uniform over the heat flux radius. Based on the experimental results, the heat flux radius for the anode and cathode for the discharge energy range 5–150 μJ are determined as follows:

$$R_{\mathrm{a}} = 0.0284 \cdot t_d^{0.9115}\ (\mu\mathrm{m}), \tag{1}$$

$$R_{\mathrm{c}} = 0.0425 \cdot t_d^{0.0895}\ (\mu\mathrm{m}), \tag{2}$$

where R_{a} and R_{c} are the heat flux radius at anode and cathode respectively, and t_d is the pulse-on-time in nanoseconds. The R-squared values for R_{a} and R_{c} are 0.9651 and 0.9301, respectively.

It has been shown by Dibitonto *et al* [12] that the fractions of energy transferred to the anode and cathode are fairly constant. An attempt has also been made by Eubank *et al* [7] to show that superheating is the main mechanism for material removal in EDM. Therefore, it is assumed in this paper that the material in the superheated area is removed completely while only a constant fraction of the material in the molten area is removed. To simplify the problem of determining the constants for the energy transferred to the anode and cathode, as well as the fraction of the molten area, a combination of these factors is used instead of treating them independently.

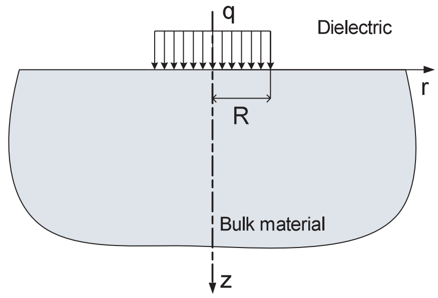

Figure 2. Schematic diagram of the electro-thermal model.

Figure 2 illustrates the schematic diagram of the model based on the aforementioned assumptions.

The governing PDE for this heat conduction problem without heat generation is given by

$$\frac{\partial^2 T}{\partial r^2} + \frac{1}{r}\frac{\partial T}{\partial r} + \frac{\partial^2 T}{\partial z^2} = \frac{1}{\alpha}\frac{\partial T}{\partial t}. \tag{3}$$

The initial condition gives

$$T(r, z, 0) = 0. \tag{4}$$

And the boundary conditions are

$$-K_{\mathrm{t}}\frac{\partial T}{\partial z} = \begin{cases} q; & 0 < r < R \\ 0; & r > R, \end{cases} \tag{5}$$

$$T(\infty, \infty, t) = 0. \tag{6}$$

Here, K_{t} is the average thermal conductivity (W m^{-1} K^{-1}) of the material and α is the thermal diffusivity of the material (m^2 s^{-1}) which can be written as

$$\alpha = \frac{K_{\mathrm{t}}}{\rho \cdot C_p}. \tag{7}$$

Here, ρ is the average material density (kg m^{-3}) and C_p is the average specific heat (J kg^{-1} K^{-1}).

The solution of the PDE is derived by using the integral transform method given by [19]

$$T(r,z,t) = \frac{q \cdot R}{2K_t} \int_0^\infty J_0(\lambda r) J_1(\lambda R) \times \left[\mathrm{e}^{(-\lambda z)} \mathrm{erfc} \left(\frac{z}{2\sqrt{\alpha t_d}} - \lambda \sqrt{\alpha t_d} \right) - \mathrm{e}^{(\lambda z)} \mathrm{erfc} \left(\frac{z}{2\sqrt{\alpha t_d}} + \lambda \sqrt{\alpha t_d} \right) \right] \frac{\mathrm{d}\lambda}{\lambda}, \tag{8}$$

where R is the heat flux radius of the anode or cathode (m), J_0 and J_1 are Bessel functions of the first kind of zero and first order, respectively, and erfc is the complementary error function.

The heat flux q is given by

$$q = \frac{C \cdot V_\mathrm{a} \cdot I_\mathrm{a}}{\pi \cdot R^2}, \tag{9}$$

where V_a is the average voltage during pulse-on-time (V), I_a is the average current during pulse-on-time (A) and C is the combination of the fraction of energy transferred and fraction of molten area for the anode or cathode. The C value is determined empirically by iterating the calculated results to agree with the experimental data. It is found that for the anode and cathode, the constants are $C_\mathrm{a} = 0.39$ and $C_\mathrm{c} = 0.14$, respectively.

Introducing dimensionless variables $u = r/R$, $w = z/R$, $\tau = (\alpha \cdot t_d)/R^2$ and $\theta(u,w,\tau) = (K_\mathrm{t} \cdot T(r,z,t))/(q \cdot R)$, a more convenient form of equation (8) can be written as

$$\theta(u,w,\tau) = \frac{1}{2} \int_0^\infty J_0(u) J_1(\lambda) \left[\mathrm{e}^{(-\lambda w)} \mathrm{erfc} \left(\frac{w}{2\sqrt{\tau}} - \lambda \sqrt{\tau} \right) - \mathrm{e}^{(\lambda w)} \mathrm{erfc} \left(\frac{w}{2\sqrt{\tau}} + \lambda \sqrt{\tau} \right) \right] \frac{\mathrm{d}\lambda}{\lambda}. \tag{10}$$

The temperature distributions in equations (8) and (10) provide a valid general solution for any radius and depth of the material. However, numerical calculations are difficult to obtain due to the infinite domain and the sinusoidal terms of the Bessel functions. Therefore, the analyses of the equation are only made in the radial and vertical axes, as shown in the following subsections.

3.1. Temperature distribution in vertical axis

Along the vertical axis ($u = 0$), Carslaw and Jaeger [19] give the temperature distribution as

$$\theta(0,w,\tau) = 2\sqrt{\tau} \left[\mathrm{ierfc} \left(\frac{w}{2\sqrt{\tau}} \right) - \mathrm{ierfc} \left(\frac{\sqrt{w^2+1}}{2\sqrt{\tau}} \right) \right]. \tag{11}$$

By using the relation between erfc and ierfc functions, equation (11) becomes

$$\theta(0,w,\tau) = 2\sqrt{\frac{\tau}{\pi}} \exp\left(-\frac{w^2}{4\tau}\right) \left[1 - \exp\left(-\frac{1}{4\tau}\right)\right] + \sqrt{w^2+1}\,\mathrm{erfc}\left(\frac{\sqrt{w^2+1}}{2\sqrt{\tau}}\right) - w\,\mathrm{erfc}\left(\frac{w}{2\sqrt{\tau}}\right). \tag{12}$$

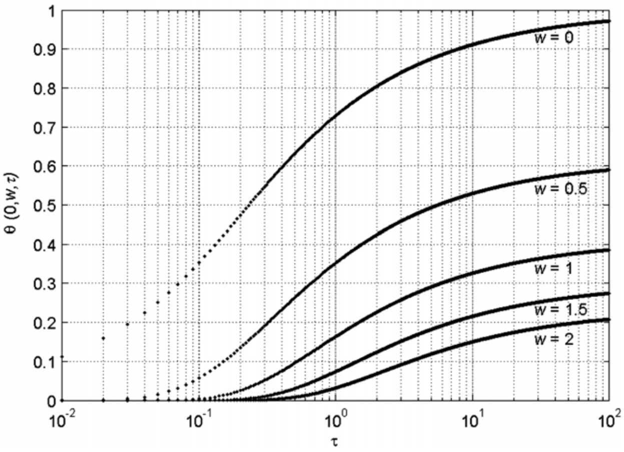

Figure 3. Dimensionless temperature versus τ at different values of w.

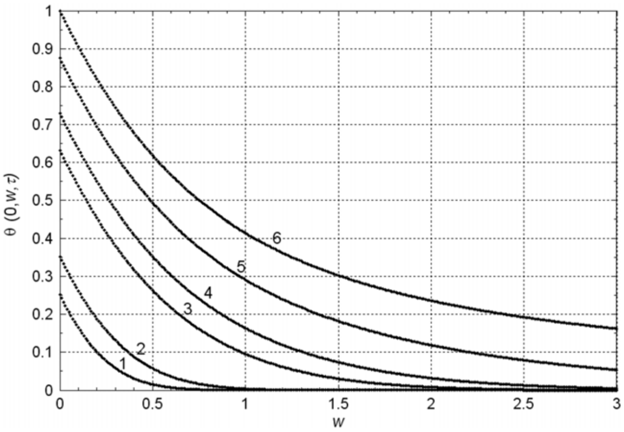

Figure 4. Dimensionless temperature versus w at different instants of time. (1) $\tau = 0.05$, (2) $\tau = 0.1$, (3) $\tau = 0.5$, (4) $\tau = 1$, (5) $\tau = 5$ and (6) $\tau = \infty$.

Equation (12) provides the dimensionless temperature distribution of the material along the vertical axis. The dimensionless temperature versus τ and w is illustrated in figures 3 and 4, respectively. The value of θ at each point on the vertical axis monotonically increases with time and gradually decreases with increasing distance from the origin. When the time goes to infinity, the temperature distribution attains the steady state with the highest temperature at the origin and given as $\theta(0,0,\infty) = 1$.

The maximum temperature of the material always occurs at the centre of the surface of the electrode being heated ($u = 0$, $w = 0$). The maximum temperature can be expressed as

$$\theta(0,0,\tau) = 2\sqrt{\frac{\tau}{\pi}} \left[1 - \exp\left(-\frac{1}{4\tau}\right)\right] + \mathrm{erfc}\left(\frac{1}{2\sqrt{\tau}}\right). \tag{13}$$

3.2. Temperature distribution in radial axis

Along the radial axis ($w = 0$), equation (10) can be written as

$$\theta(u,0,\tau) = \int_0^\infty \mathrm{erf}(\lambda\sqrt{\tau}) J_0(\lambda\rho) J_1(\lambda) \frac{\mathrm{d}\lambda}{\lambda}. \tag{14}$$

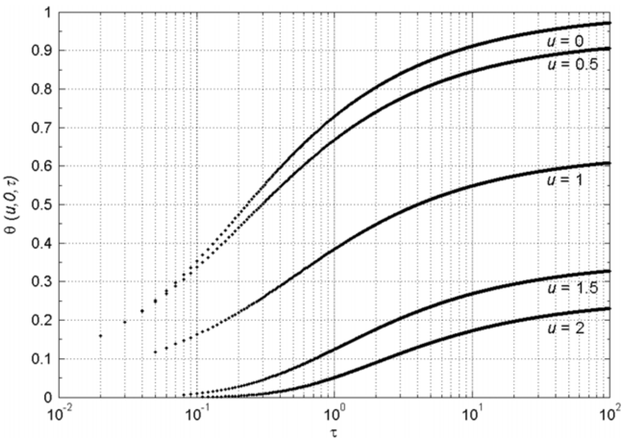

Figure 5. Dimensionless temperature versus τ at different values of u.

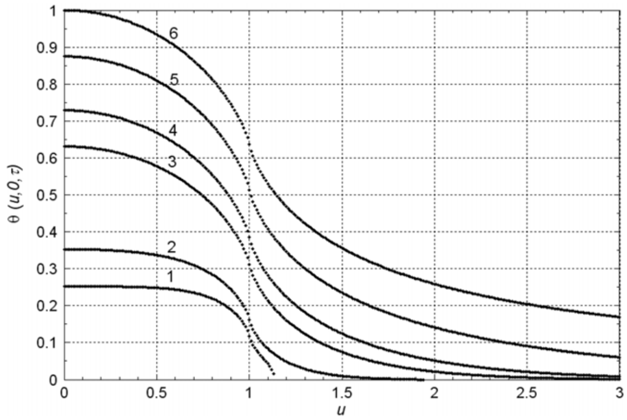

Figure 6. Dimensionless temperature versus u at different instants of time: (1) $\tau = 0.05$, (2) $\tau = 0.1$, (3) $\tau = 0.5$, (4) $\tau = 1$, (5) $\tau = 5$ and (6) $\tau = \infty$.

The relation between erfc and erf functions can be used to expand equation (14) into

$$\theta(u, 0, \tau) = \int_0^\infty J_0(\lambda u) J_1(\lambda) \frac{\mathrm{d}\lambda}{\lambda} - \int_0^\infty \operatorname{erfc}(\lambda\sqrt{\tau}) J_0(\lambda u) J_1(\lambda) \frac{\mathrm{d}\lambda}{\lambda} = I_1 - I_2. \qquad (15)$$

The first integral of equation (15) is a steady state term while the second integral is the transient term. An exact solution of the first integral is given by [20]

$$I_1 = \begin{cases} \dfrac{2}{\pi} E(u); & 0 < u < 1 \\ \dfrac{2}{\pi}; & u = 1 \\ \dfrac{2u}{\pi}[E(u^{-1}) - (1 - u^{-2}) K(u^{-1})]; & u > 1. \end{cases} \qquad (16)$$

Here, K and E are complete elliptic integrals of the first and second kind, respectively.

Following the approach taken by Beck [13], the solution for the transient term can be written as

$$I_2 = \frac{1}{2\sqrt{\pi\tau}} \sum_{i=0}^{\infty} \left\{ \frac{(-1)^i i!}{(2i+1)(4\tau)^i} \sum_{j=1}^{i+1} (i - j + 2) \times \left[\frac{u^{j-1}}{(j-1)!(i-j+2)} \right]^2 \right\}. \qquad (17)$$

Combining the calculation results of (16) and (17) into (15), the dimensionless temperature distribution along the radial axis of the material can be calculated. The dimensionless temperature versus τ and u is illustrated in figures 5 and 6, respectively.

The change in temperature with time for any point on the radial axis has a similar trend to the case of the vertical axis. For any instant of time, the highest temperature always occurs at the origin and slowly decreases with increasing distance from the centre. Near the boundary of the heat flux, where u is equal to 1, the temperature decreases abruptly and then starts to decrease gradually until it reaches zero at infinity.

4. Experimental work

The experimental work was performed by using an experimental rig which was specifically designed, built and implemented for single discharges, as shown in figure 7. The rig consisted of a 3-axis linear stage, dielectric tank and data acquisition system. A linear actuator was used to drive the linear stage. An RC single pulse generator was used to generate the spark for material removal.

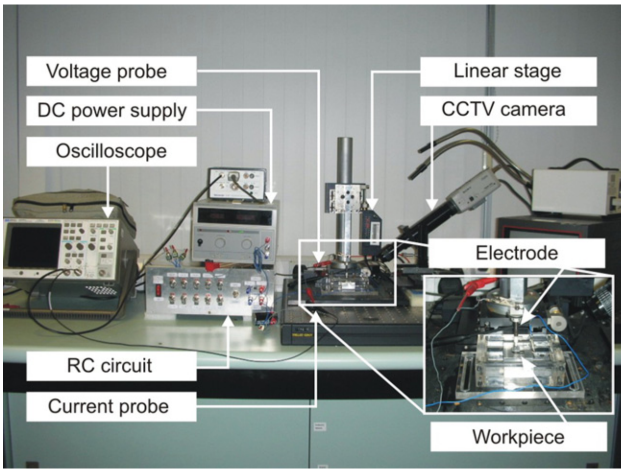

Figure 7. Single discharge experimental setup.

Table 1. Physical properties of AISI 4140.

Tensile strength	:	655 MPa (25 °C)
Average density	:	7600 kg m^{-3}
Average thermal conductivity	:	38.95 W m^{-1} K^{-1}
Average specific heat	:	473 J kg^{-1} K^{-1}
Melting temperature	:	1688 K

AISI 4140 alloy steel with the dimensions of 10 mm cube was used as the workpiece. The physical properties of the alloy steel are given in table 1. As for the electrode, pure tungsten rod with the diameter 125 μm was used. The measurements of the voltage and current from the discharge gap during the experiments were performed by using the Tektronix P5205 voltage and Tektronix CT-1 current probes. The data waveform was stored using an oscilloscope for further data processing.

Single discharge experiments were conducted by using the machining parameters shown in table 2. The polarity setting was defined by the electrical connection to the workpiece.

The gap distance was varied from 2.5 to 4.5 μm according to the energy setting. Ten replications were taken for each parameter setting to ensure the reliability of the data acquired. The dimensional geometry of micro-craters was measured using a white light interferometer. In addition, the appearance of micro-craters was analysed using scanning electron microscopy (SEM).

5. Model validation with the experimental results

The micro-craters from the experiments were analysed using SEM. The representative results are depicted in figure 8 for energy inputs of 50, 100 and 150 μJ. The craters were found to be larger for the anode as compared with the cathode.

Typical voltage and current waveforms during the discharge are shown in figure 9. Since only a fraction of the energy input, defined as discharge energy, is used during sparking, only the pulse-on-time portion of the data is used to determine the energy. From each of the waveforms acquired, the average voltage (V_a), average current (I_a) and pulse-on-time were calculated. Together with the material properties of the specimen, i.e. average thermal conductivity, average density, average specific heat and melting temperature, these data were used as input to calculate the heat flux radius (R), crater's edge temperature (θ_{crater}) and dimensionless time (τ). The crater's edge temperature works as the boundary where the material will be expelled from the superheated and molten areas, which is given as

$$\theta_{\text{crater}} = \frac{K_t(T_m - T_0)}{q \cdot R}. \tag{18}$$

Here, T_0 is the ambient temperature (K).

The vertical and radial temperature distributions are calculated by using equations (12) and (15), which are plotted together with the crater's edge temperature (θ_{crater}) to obtain the values of u and w (see figure 10). These values are then used to approximate the diameter (d), depth (h) and volume (V_{crater}) of the micro-crater where the crater volume (V_{crater}) is given as

$$V_{\text{crater}} = \frac{\pi d^2 h}{8} + \frac{\pi h^3}{6}. \tag{19}$$

Table 2. Single discharge experimental parameters.

Workpiece	:	AISI 4140 alloy steel
Electrode	:	tungsten rod
Dielectric fluid	:	synthetic electric spark oil (Daphne Cut HL-25)
Power supply voltage	:	100 V
Energy input	:	5, 25, 50, 75, 100, 125 and 150 μJ
Polarity	:	positive and negative

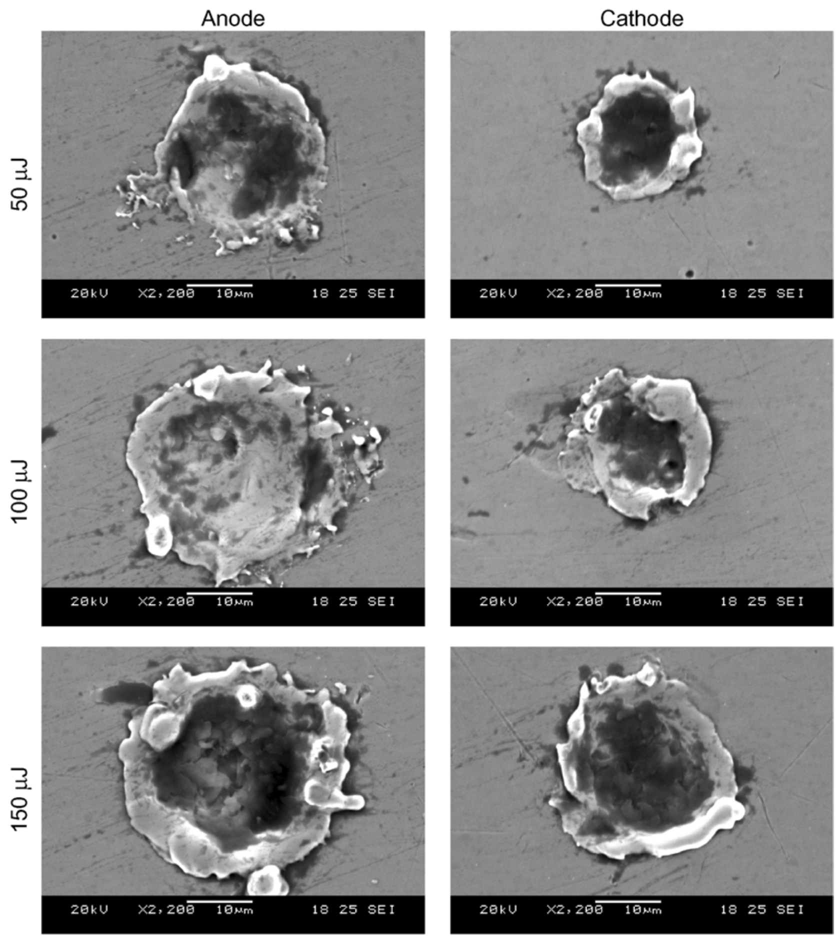

Figure 8. SEM images of micro-craters.

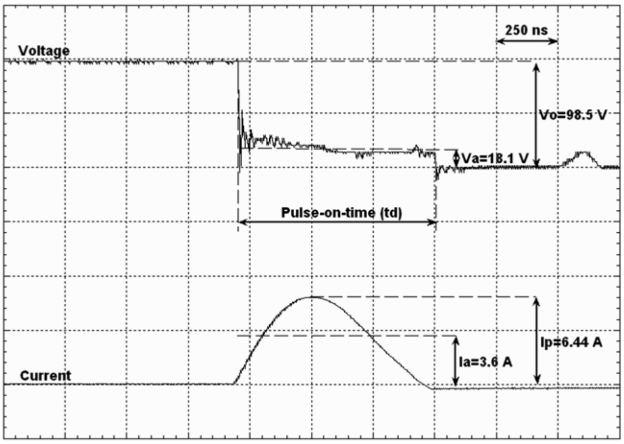

Figure 9. Voltage and current waveforms.

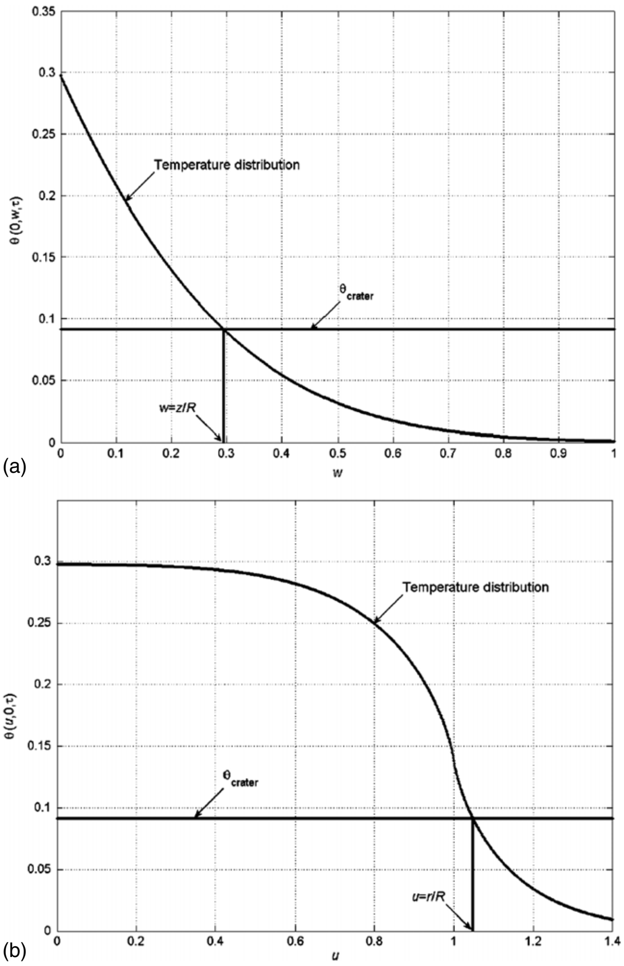

Figure 10. The vertical and radial temperature distributions of the anode: $V_a = 15.9$ V, $I_a = 2.9$ A, $t_d = 593.75$ ns and material = AISI 4140. (*a*) Vertical axis, (*b*) radial axis.

The flowchart for the calculation of crater diameter, depth and volume is given in figure 11.

The calculated results are depicted in figure 12 for pulse-on-times of 220, 430, 823 and 950 ns to illustrate differences between the crater sizes of the anode and cathode. The comparisons are made by plotting the crater depths for

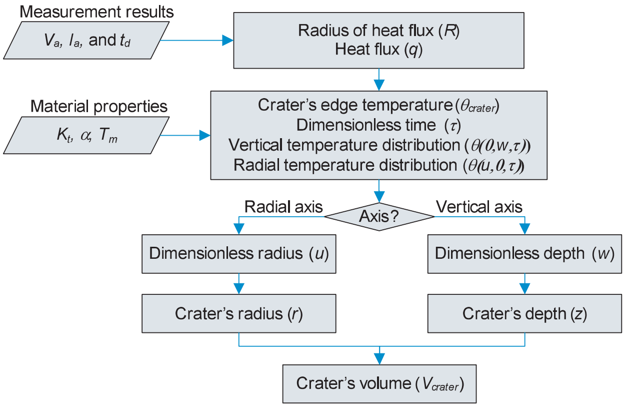

Figure 11. Flowchart for the calculation of the crater diameter, depth and volume.

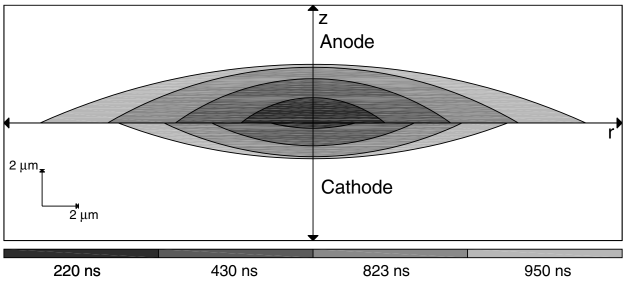

Figure 12. Comparison between the anode and cathode crater sizes for different pulse-on-times.

the anode and cathode on the positive and negative z-axis, respectively. It is evident that within this range of pulse-on-time, the craters at the anode are always larger than those at the cathode. The ratio between the anode and cathode crater diameters is 1.4 to 1.7, while the ratio for the depth is 1.6 to 4.7.

The comparisons between the theoretical and experimental results are shown in figures 13 and 14 for the anode and cathode, respectively.

The comparisons are made for the diameter, depth and volume of micro-craters. It is shown in figures 13 and 14 that the theoretical results for anode and cathode have a close agreement with the experimental results.

Table 3 presents the statistical error of the theoretical results. The comparison showed that the maximum errors for the approximation of crater diameters are 1.47 μm and 1.48 μm for the anode and cathode, respectively. As for the crater depth, the maximum errors are found to be 0.4 μm for the anode and 0.43 μm for the cathode. The errors in terms of the volumetric removal at the anode are up to 59.48 μm^3 and at the cathode up to 81.59 μm^3. In average terms, the percentage errors relative to the measurement results are found to be 3.6% for the diameter, 0.4% for the depth and 6.6% for the volume in the case of the anode. As for the cathode, the average percentage errors are found to be 0.4% for the diameter, 5.7% for the depth and 2.7% for the volume.

Thus, the comparative error approximation does not reveal any significant differences in the crater prediction between the cathode and the anode. The theoretical models for the anode and the cathode do not differ. The differences between the anode and cathode comparative results given in table 3 are largely due to the measurements of

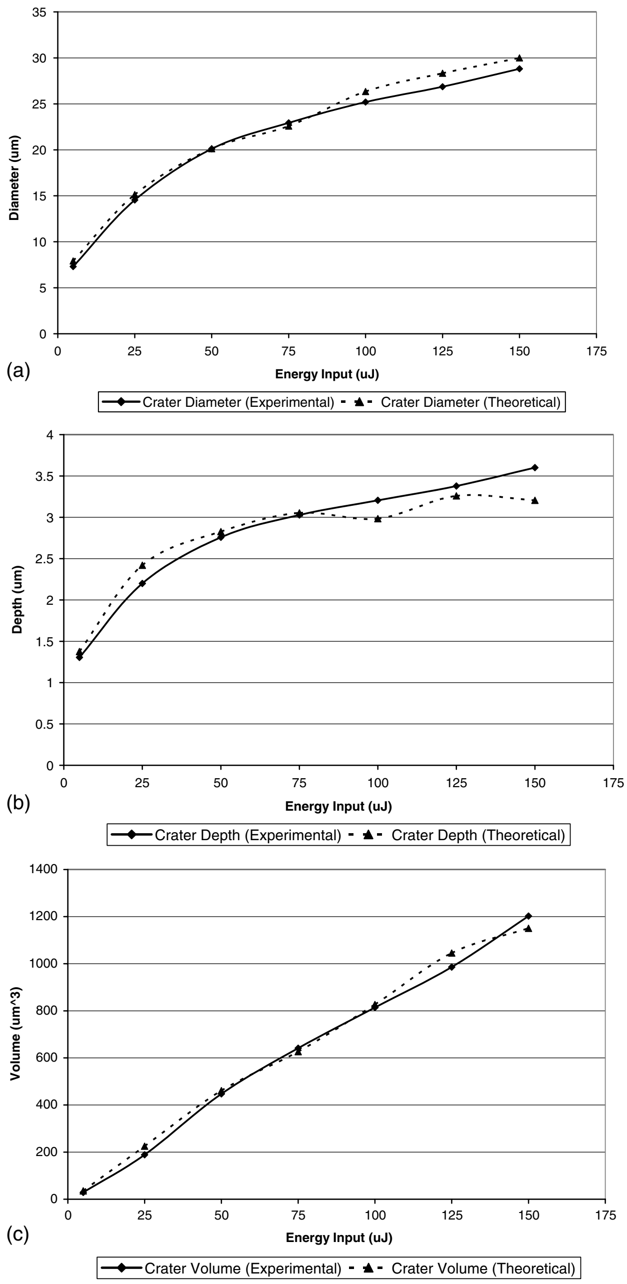

Figure 13. Comparison between theoretical and experimental results for anode (specimen: AISI 4140). (*a*) Diameter versus energy input. (*b*) Depth versus energy input. (*c*) Volume versus energy input.

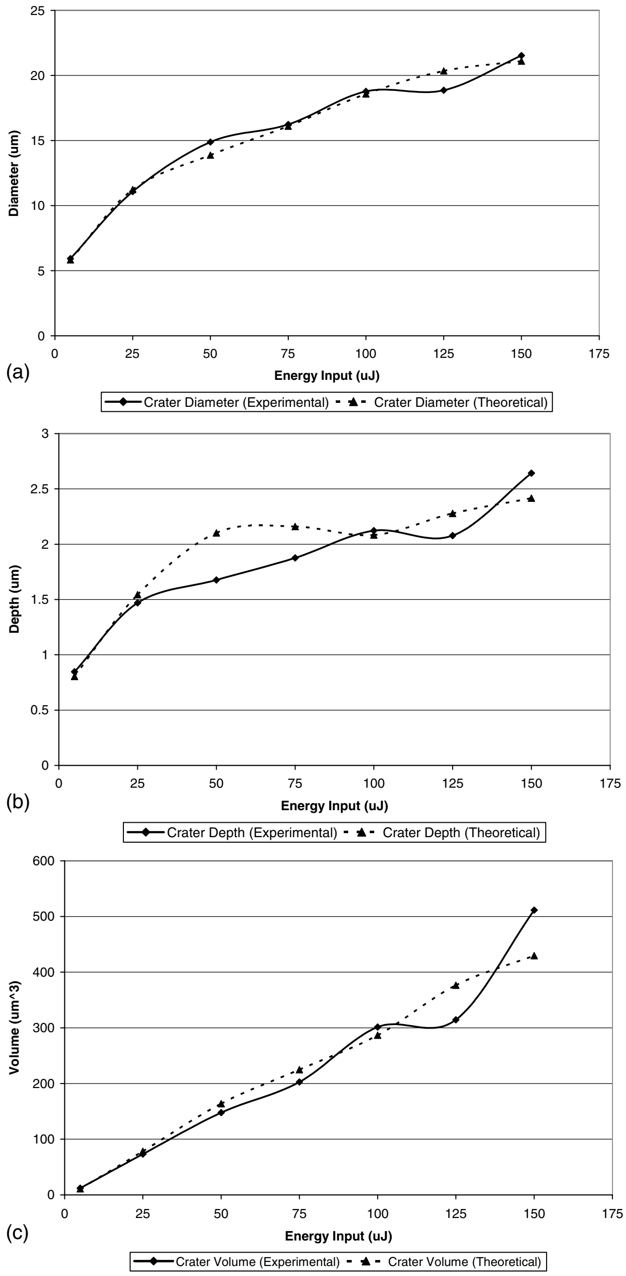

Figure 14. Comparison between theoretical and experimental results for cathode (specimen: AISI 4140). (*a*) Diameter versus energy input. (*b*) Depth versus energy input. (*c*) Volume versus energy input.

the experimental data. The irregularities in the crater geometry (see figure 8) may have contributed to the errors.

Based on the experimental results, the theoretical model developed is validated for the approximation of crater geometries at the anode and the cathode. The input energy range 5–150 μJ used in the experimental work is prevalent in the micro-EDM. Due to the approach used in this work, the reliability of the model is highly dependent on the accuracy of the empirical heat flux radius approximation. Future work will emphasize the heat flux approximation as well as a wider energy input range.

6. Conclusions

The theoretical model for the micro-EDM process has been developed based on the electro-thermal concept. The models for the temperature distribution along the vertical and radial axes are given in terms of dimensionless variables and are plotted as a general guide for the approximation of the crater geometry. The input parameters to approximate the dimensional geometry of the micro-crater are taken from the measurement results during material removal, i.e. voltage waveform, current waveform and pulse-on-time, and the material properties of the specimen, i.e. average thermal

Table 3. Statistical comparison between the theoretical and experimental results.

	Anode			Cathode		
	Diameter	Depth	Volume	Diameter	Depth	Volume
Maximum error (μm)	1.47	0.40	59.48	1.48	0.43	81.59
Average error (μm)	0.67	−0.05	8.98	0.03	0.10	1.15
Standard deviation of error (μm)	0.66	0.21	35.62	0.76	0.22	43.73
Maximum percentage error (%)	8.4	11	23.0	7.9	25.4	19.7
Average percentage error (%)	3.6	0.4	6.6	0.4	5.7	2.7

Notes: Error = experimental value − theoretical value.

$$\text{Percentage error} = \frac{(\text{experimental value} - \text{theoretical value})}{\text{experimental value}} \times 100\%.$$

conductivity, average density, average specific heat and melting temperature.

The validation of the model is achieved using a test rig for the single discharges experimental work. The comparisons between the theoretical and experimental results are done for the low energy discharges. The overall trend has shown that the theoretical model developed is valid for the approximation of crater geometry on the anode and cathode in single discharges. The model is able to predict the crater geometry within 1.47 μm for the diameter, 0.43 μm for the depth and 81.6 μm^3 for the volume. The average percentage errors between the theoretical and experimental results are found to be 3.6% for the diameter, 0.4% for the depth and 6.6% for the volume in the case of the anode. As for the cathode, the average percentage errors are found to be 0.4% for the diameter, 5.7% for the depth and 2.7% for the volume. The crater prediction between the anode and the cathode did not reveal any significant difference.

References

[1] Ho K H and Newman S T 2003 State of the art electrical discharge machining (EDM) *Int. J. Mach. Tools Manuf.* **43** 1287–300

[2] Alting L, Kimura F, Hansen H N and Bissacco G 2003 Micro engineering *CIRP Ann.—Manuf. Technol.* **52** 635–57

[3] Han F, Yamada Y, Kawakami T and Kunieda M 2006 Experimental attempts of sub-micrometer order size machining using micro-EDM *Precision Eng.* **30** 123–31

[4] Yeo S H and Murali M 2003 A new technique using foil electrodes for the electro-discharge machining of micro grooves *J. Micromech. Microeng.* **13** 1–5

[5] Nexus 2005 *NEXUS MST/MEMS Market Analysis* III 2005-2009

[6] Boothroyd G G 2006 *Fundamentals of Machining and Machine Tools* 3rd edn (Boca Raton, FL: CRC/Taylor and Francis)

[7] Eubank P T, Patel M R, Burrufet M A and Bozkurt B 1993 Theoretical models of the electrical discharge machining process: III. The variable mass, cylindrical plasma model *J. Appl. Phys.* **73** 7900–9

[8] Lhiaubet C, Benzerga L and Boyer L 1986 Simulation of the EDM process modeled as a semi-infinite solid *Modeling, Sensing, and Control of Manufacturing Processes (DSC vol 4), Presented at the Winter Annual Meeting of the American Society of Mechanical Engineers (New York, NY, USA)* (Anaheim, CA, USA: ASME)

[9] Dhanik S and Joshi S S 2005 Modeling of a single resistance capacitance pulse discharge in micro-electro discharge machining *J. Manuf. Sci. Eng., Trans. ASME* **127** 759–67

[10] Snoeys R and Van Dijck F 1971 Investigation of electro discharge machining operations by means of thermo-mathematical model *CIRP Ann.* **20** 35–7

[11] Van Dijck F S and Dutre W L 1974 Heat conduction model for the calculation of the volume of molten metal in electric discharges *J. Phys. D: Appl. Phys.* **7** 899–910

[12] DiBitonto D D, Eubank P T, Patel M R and Barrufet M A 1989 Theoretical models of the electrical discharge machining process. I. A simple cathode erosion model *J. Appl. Phys.* **66** 4095–103

[13] Beck J V 1981 Large time solutions for temperatures in a semi-infinite body with a disk heat source *Int. J. Heat Mass Transfer* **24** 155–64

[14] Beck J V 1981 Transient temperatures in a semi-infinite cylinder heated by a disk heat source *Int. J. Heat Mass Transfer* **24** 1631–40

[15] Pandey P C and Jilani S T 1986 Plasma channel growth and the resolidified layer in EDM *Precision Eng.* **8** 104–10

[16] Jilani S T and Pandey P C 1983 Analysis of surface erosion in electrical discharge machining *Wear* **84** 275–84

[17] Patel M R, Barrufet M A, Eubank P T and DiBitonto D D 1989 Theoretical models of the electrical discharge machining process: II. The anode erosion model *J. Appl. Phys.* **66** 4104–11

[18] Shobert E I 1983 What happens in EDM *Electrical Discharge Machining: Tooling, Methods, and Applications* (Dearborn, MI: Society of Manufacturing Engineers) pp 3–4

[19] Carslaw H S and Jaeger J C 1986 *Conduction of Heat in Solids* 2nd edn (Oxford: Clarendon)

[20] Thomas P H 1957 Some conduction problems in the heating of small areas on large solids *Q. J. Mech. Appl. Math.* **10** 482–93